PERGAMON

International Journal of Solids and Structures 40 (2003) 6189–6209

INTERNATIONAL JOURNAL OF SOLIDS and STRUCTURES

www.elsevier.com/locate/ijsolstr

Creep simulation of asymmetric effects by use of stress mode dependent weighting functions

Rolf Mahnken *

University of Paderborn, Warburger Street 100, D-33098 Paderborn, Germany

Abstract

The paper presents a framework for creep modeling of materials exhibiting different behaviors in different loading scenarios, such as tension, compression and shear, respectively. To this end an additive decomposition of the flow rule is assumed into a sum of weighted stress mode related quantities. The characterization of the stress modes is obtained in the octahedral plane of the deviatoric stress space in terms of a single scalar variable, such that stress mode dependent scalar weighting functions can be constructed. Furthermore the numerical implementation into a finite element program of the resulting set of constitutive equations and aspects of the sensitivity analysis for parameter identification are addressed. Verification of the constitutive equations is succeeded for an aluminum alloy AK4-1T and a superalloy René 95, respectively. In two finite element examples the proposed model is applied to investigate the relaxation behavior of a square plate with circular hole and the evolution of creep damage in a gasturbine blade subjected to centrifugal and thermal loads.

Keywords: Creep; Asymmetric effects; Creep damage; Superalloys; Numerical integration; Finite elements; Parameter identification

1. Introduction

Creep is a phenomenon of progressive deformation of solid materials subjected to constant stress at elevated temperatures. Dependent on the amount of stress and temperature the creep mechanisms within the microstructure for metallic materials can be grouped into dislocation glide, dislocation creep, diffusion creep and grain boundary sliding, see e.g. Ashby and Jones (1996, p. 187 ff), Dieter (1988, p. 445 ff), Riedel (1987, p. 3 ff). Typically the resulting experimental effects exhibit the three stages of primary, secondary and tertiary creep. The model development for the design of engineering structures then very often is based on one type of experiment, where e.g. a tension test is a favorite type for metals.

However, extended experimental tests for many metallic materials exhibit different creep behaviors for different loading types such as tension, compression and shear. For example test results for a superalloy René 95 in Stouffer and Dame (1996, p. 116), show, that for merely the same magnitudes of stress in tension and compression the magnitudes of creep rates in tension are much greater than the corresponding rates in

* Tel.: +49-5251-602283; fax: +49-5251-603483.
E-mail address: rolf.mahnken@ltm.uni-paderborn.de (R. Mahnken).

0020-7683/$ - see front matter © 2003 Elsevier Ltd. All rights reserved.
doi:10.1016/S0020-7683(03)00388-3

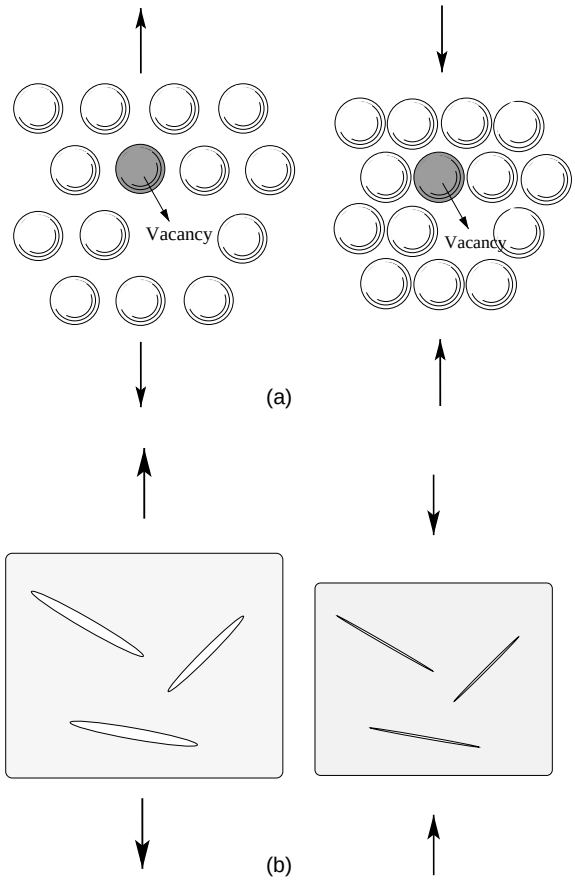

Fig. 1. Metallographic causes of asymmetry: (a) Influence of diffusion: tensile stresses expand the lattice and reduce the resistance to diffusion, whereas compressive stresses reduce the lattice dimensions and increase the resistance to diffusion. (b) Influence of microcracks: cracks that are closed have only a small influence on the creep behavior under uniaxial compression, whereas in uniaxial tension the creep rate in general is much greater.

compression. As illustrated in Fig. 1 two metallographical explanations can be summarized as the main sources of this effect.

To explain the first source we recall that diffusion is the dominate deformation mechanism of creep. Then, tensile stresses expand the lattice and reduce the resistance to diffusion, whereas compressive stresses reduce the lattice dimensions and increase the resistance for diffusion. The second source is due to the progressive material deterioration of creep damage, where dependent on the amount of stress and temperature, the microdefects can be grouped into microcracks, voids and pores. The resulting macromechanical mechanisms, even if isotropic, may be different for different stress modes. For example, microcracks that are closed have only a small influence on the creep behavior under uniaxial compression, whereas in uniaxial tension the creep rate in general is much greater. It is also noteworthy that in addition to the above mentioned characteristics in tension and compression a pure shear test may show a further independent response.

The above phenomena are, from a more general point of view, examples of so-called *asymmetric effects* or as denoted by Altenbach et al. (1995) *non-classical* effects. These are defined by the observation, that a certain

type of experiment, such as a tension test, is not sufficient in order to characterize the material for different loading scenarios. Instead, additional *independent* types of experiments, such as compression, shear and hydrostatic tests, are necessary in order to get a more comprehensive (though in general still not complete) characterization of the material. It should be emphasized, that the asymmetric effects examined in this paper are restricted to *isotropic* materials, and therefore carefully have to be distinguished from the effects of initial (material) anisotropy and induced anisotropy (such as a Bauschinger effect or damaged induced anisotropy).

Several publications can be found in the literature for simulation of inelastic material behavior with asymmetric effects. Many of these approaches are based on a stress potential dependent on the stress tensor and further state variables, which describe e.g. the state of hardening, softening or damage, respectively. Typically, dependent on the symmetry of the considered material (e.g. isotropy, cubic, transversal symmetry) polynomial invariants of the stress tensor are incorporated into the potential. Along this line constitutive equations within the field of plasticity have been formulated e.g. in Spitzig et al. (1975), Altenbach (2001), Altenbach et al. (1995), Mahnken (2001), Zolochevskii (1989) amongst others. Approaches for asymmetric effects in creep are suggested in Altenbach et al. (1995), Betten et al. (1998), Voyiadjis and Zolochevsky (1998), Voyiadjis and Zolochevsky (2000), Zolochevsky (1991) amongst others.

It appears from the above mentioned references that so far no common approach exists concerning the best strategy for taking account individual loading scenarios in the constitutive equations. A general agreement is the incorporation of odd power terms for odd invariants of stresses, see e.g. Spitzig et al. (1975), Betten et al. (1999). Furthermore, a scalar variable, which is expressed in terms of the ratio of the second and third basic invariant of the deviatoric stress tensor, can be used as an indicator for detection of differences in the loading modes. This quantity, which will be called *stress mode angle* in this work, has been applied e.g. in Zolochevskii (1990), Altenbach (2001), Ehlers (1995), Mahnken (2001).

This work makes extensive use of the *stress mode angle* for creep modeling with asymmetric effects. The key idea consists in an additive decomposition of the inelastic strain rate, where each of the related quantities incorporates a weighting function dependent on the *stress mode angle*. The advantage of this approach is, that certain (though not all) material parameters, such as Norton-type constants, can be obtained individually from specific loading modes such as tension, compression and shear, investigated experimentally in the laboratory.

A further part of the paper is devoted to the numerical implementation of the constitutive relations, which, regarding asymmetric inelastic effects, seems to have attracted little attention in the literature so far. In particular the derivation of the algorithmic tangent operator for the equilibrium iteration and the sensitivity terms for parameter identification, each of them consistent with the underlying integration algorithm, are derived. The proposed integration algorithm and the algorithmic tangent operator have been implemented into a general finite element program such as the UMAT subroutine of the commercial program (ABAQUS-Version 6.3, 2002).

The structure of the paper is as follows: Section 2 presents a general framework for stress mode dependent creep. In Section 3 stress mode related weighting functions are introduced, which are incorporated into a prototype model of Section 4. Aspects of the numerical implementation into general finite element programs and into gradient-based optimization programs for parameter identification are outlined in Section 5. In Section 6 four examples exhibiting asymmetric effects are presented: in the first two examples verification of the constitutive equations is succeeded for an aluminum alloy AK4-1T and a superalloy René 95, respectively. Furthermore, in two finite element examples the proposed model is applied to investigate the relaxation behavior of a square plate with circular hole and the evolution of creep damage in a gasturbine blade.

1.1. Notations

Square brackets $[\bullet]$ are used throughout the paper to denote 'function of' in order to distinguish from mathematical groupings with parenthesis $(\bullet)$.

2. A general framework for stress mode dependent creep

In the remainder of this work the standard additive decomposition of the second-order total strain tensor $\boldsymbol{\varepsilon}$ is assumed, i.e.

$$\boldsymbol{\varepsilon} = \boldsymbol{\varepsilon}^{\mathrm{el}} + \boldsymbol{\varepsilon}^{\mathrm{in}} \tag{1}$$

Here, as usual the elastic strain tensor $\boldsymbol{\varepsilon}^{\mathrm{el}}$ is related to the stress tensor $\boldsymbol{\sigma}$ by Hooke's law

$$\boldsymbol{\sigma} = \mathbb{C} : \boldsymbol{\varepsilon}^{\mathrm{el}} \tag{2}$$

where $\mathbb{C}$ is the fourth-order elasticity tensor. The second-order inelastic strain tensor $\boldsymbol{\varepsilon}^{\mathrm{in}}$ is obtained from evolution equations for the strain rate tensor $\dot{\boldsymbol{\varepsilon}}^{\mathrm{in}}$, where $\dot{(.)}$ represents the time derivative. Many publications have been devoted to the issue of formulating appropriate evolution equations. An extensive overview on different concepts, such as the creep potential theory and the tensor function theory, has recently been published by Betten (2001).

In the following exposition a *stress mode* related approach according to the following structure is proposed:

$$\begin{aligned}
&1.\ \dot{\boldsymbol{\varepsilon}}^{\mathrm{in}} = \sum_{i=1}^{S} w_i \dot{F}_i \mathbf{d}_i, \quad \text{where} \\
&2.\ \dot{F}_i = \dot{F}_i[\boldsymbol{\sigma}, \mathbf{q}, \ldots; \boldsymbol{\kappa}] \\
&3.\ \mathbf{d}_i = \mathbf{d}_i[\boldsymbol{\sigma}, \mathbf{q}, \ldots; \boldsymbol{\kappa}] \\
&4.\ \dot{\mathbf{q}} = \dot{\mathbf{q}}[\boldsymbol{\sigma}, \mathbf{q}, \ldots; \boldsymbol{\kappa}] \\
&5.\ w_i = w_i[\boldsymbol{\sigma}]
\end{aligned} \tag{3}$$

Eq. (3.1) represents the additive decomposition of the inelastic strain rate tensor into S stress mode related quantities. Each of them incorporates a scalar *flow factor* $\dot{F}_i$ and a tensorial *flow direction* $\mathbf{d}_i$, both dependent on the stress tensor $\boldsymbol{\sigma}$, a set of structural (internal) variables $\mathbf{q}$ and also a vector of material parameters $\boldsymbol{\kappa}$. Furthermore, in the above skeleton structure (3) a weighting function w_i is associated to each mode i, which is dependent on the stress tensor $\boldsymbol{\sigma}$, and for which it is stipulated that

$$\begin{aligned}
&1.\ \sum_{i=1}^{S} w_i[\boldsymbol{\sigma}] = 1 \\
&2.\ w_i[\boldsymbol{\sigma}_j] = \delta_{ij}
\end{aligned} \tag{4}$$

Here the stress tensors $\boldsymbol{\sigma}_i$, $i = 1, 2, \ldots, S$ refer to independent characteristic *stress modes*, which for example can be investigated experimentally in tension, compression and shear, respectively. Furthermore we remark, that Eq. (4.1) can be regarded as a *completeness condition*, whereas Eq. (4.2) constitutes a *normalization condition* for the weighting functions.

The above Eqs. (3) are regarded as very general, thus including also anisotropic material behavior. In particular these can be viewed as an extension of the framework based on elastic projection operators, see e.g. Mahnken (2002) and references therein. However, in the sequel of this work we restrict ourselves to isotropic materials, and the aspect of anisotropy combined to stress mode dependent material behavior shall be regarded at a later stage.

3. Stress mode related weighting functions

In the remainder of this work, we will concentrate on the three independent stress modes for tension, compression and shear with applications to isotropic materials. Following the same procedure as extensively outlined by Ehlers (1995), these modes can be represented in the octahedral plane of the associated deviatoric stress tensor. To this end the quantities

$$\begin{aligned} &1.\ \theta = \frac{1}{3}\arccos[\xi], \quad \text{where} \\ &2.\ \xi = \frac{\sqrt{27}}{2}\frac{J_3}{(J_2)^{3/2}} \\ &3.\ J_i = \frac{1}{i}\mathbf{1} : \boldsymbol{\sigma}^i_{\mathrm{dev}}, \quad i = 2,3 \end{aligned} \tag{5}$$

are defined. Here θ shall be referred to as the *stress mode angle* dependent on the *stress mode factor* ξ. Furthermore in the above Eq. (5.3) J_2 and J_3 denote the second and third basic invariant of the deviatoric stress tensor $\boldsymbol{\sigma}_{\mathrm{dev}}$, respectively, and the second-order unity tensor $\mathbf{1}$ has been introduced.

A graphical interpretation of the stress mode angle θ is given at the top of Fig. 2. In particular it becomes apparent, that the independent stress modes of tension, compression and shear are characterized by the stress mode angles

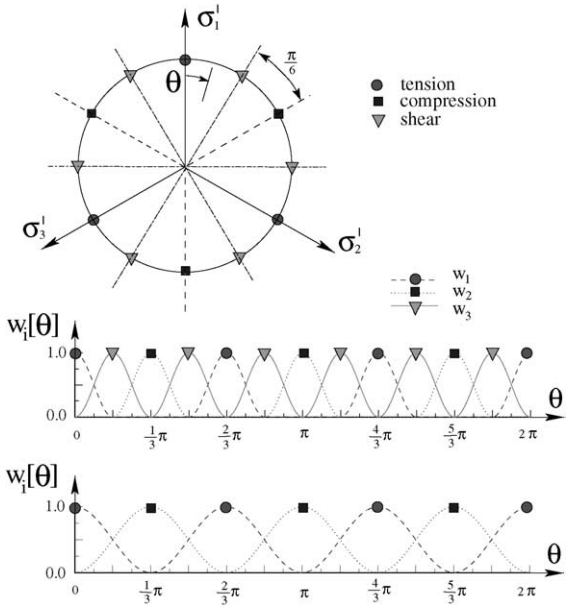

Fig. 2. Top: Octahedral plane in the deviatoric stress space. Here σ'_1, σ'_2, σ'_3 denote the principal deviatoric stresses. Circles, squares and triangles represent stress modes of tension, compression, and shear, respectively. Middle: Weighting functions (9) in terms of the stress mode angle θ for tension, compression and shear mode. Bottom: Weighting functions (10) in terms of the stress mode angle θ for tension and compression.

$$\begin{aligned}
&\text{1. tension:} && \theta_1 = \frac{2\pi}{3} n, \quad n = 0, 1, 2, \dots \\
&\text{2. compression:} && \theta_2 = \frac{2\pi}{3} n + \frac{\pi}{3}, \quad n = 0, 1, 2, \dots \\
&\text{3. shear:} && \theta_3 = \frac{\pi}{3} n + \frac{\pi}{6} \quad n = 0, 1, 2, \dots
\end{aligned} \tag{6}$$

and for each of the stress modes the following periodicity angles

$$\begin{aligned}
&\text{1. tension:} && \tilde{\theta}_1 = \frac{2\pi}{3} \\
&\text{2. compression:} && \tilde{\theta}_2 = \frac{2\pi}{3} \\
&\text{3. shear:} && \tilde{\theta}_3 = \frac{\pi}{3}
\end{aligned} \tag{7}$$

are obtained. Based on these observations, in addition to the relations (4) the following is required for the weighting functions

$$\begin{aligned}
&1. \ \sum_{i=1}^{S} w_i[\theta] = 1 \\
&2. \ w_i[\theta_j] = \delta_{ij} \\
&3. \ w_i[\theta] = w_i[\theta + \tilde{\theta}_i]
\end{aligned} \tag{8}$$

For the stress modes related to the loading scenarios of tension, compression and shear, we set $S = 3$ and the requirements (8) are satisfied by the following weighting function

$$\begin{aligned}
&\text{1. tension:} && w_1[\theta] = \begin{cases} \frac{1}{2} + \frac{1}{2}\cos 3\theta, & \text{if } -\frac{\pi}{6} + n\tilde{\theta}_1 \leqslant \theta \leqslant \frac{\pi}{6} + n\tilde{\theta}_1 \\ 0, & \text{else} \end{cases} \\
&\text{2. compression:} && w_2[\theta] = \begin{cases} 0, & \text{if } -\frac{\pi}{6} + n\tilde{\theta}_1 \leqslant \theta \leqslant \frac{\pi}{6} + n\tilde{\theta}_1 \\ \frac{1}{2} + \frac{1}{2}\cos 3\theta, & \text{else} \end{cases} \\
&\text{3. shear:} && w_3[\theta] = \frac{1}{2} + \frac{1}{2}\cos(3\theta - \pi)
\end{aligned} \tag{9}$$

and where $n = 0, 1, 2, \dots$ are integer values. A graphical representation of the weighting functions (9) is given in the middle graph of Fig. 2. For the case, that experimental data are available only for loading in tension and compression with $S = 2$, the following weighting functions can be used

$$\begin{aligned}
&\text{1. tension:} && w_1[\theta] = \frac{1}{2} + \frac{1}{2}\cos 3\theta \\
&\text{2. compression:} && w_2[\theta] = \frac{1}{2} + \frac{1}{2}\cos(3\theta - \pi)
\end{aligned} \tag{10}$$

These functions, which are illustrated at the bottom of Fig. 2, do also satisfy the requirements (8).

Upon using the definition (5.1), alternatively the functional relationships (9) and (10) can be rewritten in terms of the stress mode factor ξ as

$$\begin{aligned} &\text{1. tension:} && w_1[\xi] = \begin{cases} \xi^2, & \text{if } \xi \geqslant 0 \\ 0, & \text{else} \end{cases} \\ &\text{2. compression:} && w_2[\xi] = \begin{cases} 0, & \text{if } \xi \leqslant 0 \\ \xi^2, & \text{else} \end{cases} \\ &\text{3. shear:} && w_3[\xi] = 1 - \xi^2 \end{aligned} \tag{11}$$

or

$$\begin{aligned} &\text{1. tension:} && w_1[\xi] = \frac{1}{2}(1+\xi) \\ &\text{2. compression:} && w_2[\xi] = \frac{1}{2}(1-\xi) \end{aligned} \tag{12}$$

respectively.

4. A prototype model for stress mode dependent creep

It is the object of this section to present a specific example of the general framework (3) for creep modeling. The complete set of equations is summarized in Table 1, and some specific comments on the constitutive equations are discussed next:

4.1. Remarks

1. Concerning notation in Eq. (I) of Table 1, the fourth-order projection tensor $I\!I^{\mathrm{dev}} = I\!I - 1/3\mathbf{1} \otimes \mathbf{1}$ is defined, where II and **1** are fourth-order and second-order unit tensor, respectively.
2. The generality of Eqs. (3) is not fully exploited. This is done in order to reduce the resulting number of material parameters. In this respect the flow direction $\boldsymbol{d}$ is assumed to be identical for all stress modes; only a dependency of the flow factor $\dot{F}_t$ on the different stress modes is assumed. Furthermore for simplicity merely *one* isotropic scalar variable R is introduced, which is related to *all* stress modes.
3. The constants A_i and n_i in the damage independent part of Eq. V in Table 1 are material parameters associated to the ith mode, thus yielding a Norton–Bailey structure for each flow parameter $\dot{F}_i$. This relation is motivated by a linear "$\log(\sigma)$ vs. $\log(\dot{\varepsilon})$" relation in the secondary creep phase, see e.g. Poirier (1985).
4. Many materials show a deviation from the linear "$\log(\sigma)$ vs. $\log(\dot{\varepsilon})$" relation in the secondary creep phase, and this effect is referred to as *power-law-breakdown*, see e.g. Poirier (1985, p. 81). Then, very often it is appropriate to replace the Norton–Bailey ansatz by a Garofalo ansatz as

$$\dot{F}_i = A_i(\sinh \alpha_i \sigma_v)^{n_i}, \quad i = 1, \ldots, S \tag{13}$$

   and where A_i, α_i and n_i are material parameters associated to each mode.
5. As mentioned in the introduction, creep is typically accompanied by progressive material deterioration due to creep damage. A large amount of literature exist on this phenomenon, where also much interest has been directed to anisotropic damage effects. In our prototype model a simple isotropic damage ansatz of Kachanow–Rabotnow type is introduced. Note, that the intensity of the damage state d_t on the different modes in Eq. (V) of Table 1 can be influenced by the material parameters p_i. In this respect it is reasonable to set $p_i \geqslant 0$ for a tension mode and $p_i = 0$ for a compression mode, where the latter choice takes into account closure effects.

Table 1
Constitutive relations for stress mode dependent creep

I. Kinematic decomposition

$$\boldsymbol{\varepsilon} = \boldsymbol{\varepsilon}^{\mathrm{el}} + \boldsymbol{\varepsilon}^{\mathrm{in}}$$

II. Hooke's law

$$\boldsymbol{\sigma} = \mathbb{C} : \boldsymbol{\varepsilon}^{\mathrm{el}} = 2GII^{\mathrm{dev}} : \boldsymbol{\varepsilon}^{\mathrm{el}} + B\mathbf{1} : \boldsymbol{\varepsilon}^{\mathrm{el}}\mathbf{1}$$

III. Inelastic strain evolution

1. $\dot{\boldsymbol{\varepsilon}}^{\mathrm{in}} = \dot{F}_t\mathbf{d}$
2. $\dot{F}_t = \sum_{i=1}^{S} w_i\dot{F}_i$

IV. Flow direction

1. $\mathbf{d} = \dfrac{3}{2\sigma_v}\boldsymbol{\sigma}_{\mathrm{dev}}$
2. $\sigma_v^2 = \dfrac{3}{2}\boldsymbol{\sigma}_{\mathrm{dev}} : \boldsymbol{\sigma}_{\mathrm{dev}} = 3J_2$

V. Flow factor associated to each mode

$$\dot{F}_i = A_i\left(\frac{\sigma_v - R}{\sigma_0}\right)^{n_i}\left(\frac{1}{1-d_t}\right)^{p_i}, \quad i = 1,\ldots,S$$

VI. Damage evolution

$$\dot{d}_t = \sum_{i=1}^{S} w_i\dot{d}_i$$

VII. Damage factor associated to each mode

$$\dot{d}_i = B_i\left(\frac{\sigma_v}{\sigma_0}\right)^{m_i}\left(\frac{1}{1-d_t}\right)^{q_i}, \quad i = 1,\ldots,S$$

VIII. Isotropic hardening variable

$$R[e_v] = q(1 - \exp(-se_v))$$

IX. Equivalent inelastic strain

$$\dot{e}_v^2 = \frac{2}{3}\dot{\boldsymbol{\varepsilon}}^{\mathrm{in}} : \dot{\boldsymbol{\varepsilon}}^{\mathrm{in}} = \dot{F}_t^2$$

X. Material parameters

$$\boldsymbol{\kappa} = [A_i, n_i, p_i, B_i, m_i, q_i, \{i = 1,\ldots,S\}, q, s]^{\mathrm{T}}$$

The weighting functions w_i are specified in Eqs. (9) and (10), respectively.

6. All material constants of the prototype model characterizing the inelastic behavior of the model are summarized in Eq. (X) of Table 1. In addition to the elastic constants, the shear module G and the bulk module B, respectively, these have to be calibrated on the basis of experimental data. In order to be physically meaningful they are restricted to lower and upper bounds a_k, b_k, respectively. These constraints then define the feasible domain $\mathscr{K}$, such that

$$\boldsymbol{\kappa} \in \mathscr{K} \subset \mathbb{R}^{n_p}, \quad \mathscr{K} := \{\boldsymbol{\kappa} : a_k \leqslant \kappa_k \leqslant b_k, k = 1,\ldots,n_p\} \tag{14}$$

where $n_p = \dim[\boldsymbol{\kappa}]$ denotes the number of material parameters for our specific model. We also remark, that the constant σ_0 in Eqs. (V) and (VII) of Table 1 has the interpretation of a normalization variable, and thus is not regarded as an independent material parameter.

5. Numerical implementation

This section is concerned with numerical integration of the rate-equations for $\boldsymbol{\varepsilon}^{\text{in}}$ and d_t in Table 1. Following standard integration procedures in finite element techniques a *strain-driven* algorithm is considered, where the total strain tensor ${}^{n+1}\boldsymbol{\varepsilon}$ and initial values ${}^{n}\boldsymbol{\varepsilon}^{\text{in}}$, ${}^{n}d_t$ at each time step ${}^{n+1}t$ are given. Then it is the object to find the corresponding quantities ${}^{n+1}\boldsymbol{\varepsilon}^{\text{in}}$, ${}^{n+1}d_t$ at time ${}^{n+1}t$ consistent with the constitutive equations of the previous sections. In order to alleviate the notation, the index $n+1$, referring to the actual time step, will be omitted subsequently.

5.1. Integration scheme

For numerical integration of the rate-equations for $\boldsymbol{\varepsilon}^{\text{in}}$ and d_t summarized in Table 1 an Euler backward rule renders the following update scheme:

$$\begin{aligned} &1.\ \boldsymbol{\varepsilon}^{\text{in}} = {}^{n}\boldsymbol{\varepsilon}^{\text{in}} + \Delta\boldsymbol{\varepsilon}^{\text{in}} \\ &2.\ d_t = {}^{n}d_t + \Delta d_t \end{aligned} \tag{15}$$

Here the increments on the r.h.s in the above equations are obtained from

$$\begin{aligned} &1.\ \Delta\boldsymbol{\varepsilon}^{\text{in}} = \Delta F_t \mathbf{d} \\ &2.\ \Delta F_t = \sum_{i=1}^{S} \Delta F_i w_i \\ &3.\ \Delta F_i = \Delta t A_i \left(\frac{\sigma_v - R}{\sigma_0}\right)^{n_i} \left(\frac{1}{1-d_t}\right)^{p_i} \\ &4.\ w_i = w_i[\xi] \text{ (see Eqs. (11) and (12))} \\ &5.\ \sigma_v^2 = \frac{3}{2}\boldsymbol{\sigma}_{\text{dev}} : \boldsymbol{\sigma}_{\text{dev}} = 3J_2 \\ &6.\ \mathbf{d} = \frac{3}{2\sigma_v}\boldsymbol{\sigma}_{\text{dev}} \\ &7.\ R = q(1 - \exp(-se_v)) \\ &8.\ e_v = {}^{n}e_v + \Delta e \\ &9.\ \Delta e = \Delta F_t \\ &10.\ \Delta d_t = \sum_{i=1}^{S} \Delta d_i w_i \\ &11.\ \Delta d_i = \Delta t B_i \left(\frac{\sigma_v}{\sigma_0}\right)^{m_i} \left(\frac{1}{1-d_t}\right)^{q_i} \end{aligned} \tag{16}$$

and where $\Delta t = {}^{n+1}t - {}^{n}t$ denotes the time increment. Upon combining Eqs. (15.1), (16.1) and (16.6) with Eqs. (I) and (II) of Table 1 the deviatoric part of the stress tensor is obtained from the relations

$$\begin{aligned} &1.\ \boldsymbol{\sigma}_{\text{dev}} = \boldsymbol{\sigma}_{\text{dev}}^{\text{tr}} - \frac{3G\Delta F_t}{\sigma_v}\boldsymbol{\sigma}_{\text{dev}}, \quad \text{where} \\ &2.\ \boldsymbol{\sigma}_{\text{dev}}^{\text{tr}} = 2G(\boldsymbol{\varepsilon}_{\text{dev}} - {}^{n}\boldsymbol{\varepsilon}^{\text{in}}) \end{aligned} \tag{17}$$

and where $\boldsymbol{\sigma}_{\text{dev}}^{\text{tr}}$ is typically referred to as the trial stress tensor, see e.g. Simo and Hughes (1998) and references therein. The above representation (17.1) shows, that $\boldsymbol{\sigma}_{\text{dev}}$ and $\boldsymbol{\sigma}_{\text{dev}}^{\text{tr}}$ are coaxial, and this induces the relation

$$\frac{\boldsymbol{\sigma}_{\mathrm{dev}}}{\sigma_v}=\frac{\boldsymbol{\sigma}^{\mathrm{tr}}_{\mathrm{dev}}}{\sigma^{\mathrm{tr}}_v}\Rightarrow \boldsymbol{\sigma}_{\mathrm{dev}}=\frac{\sigma_v}{\sigma^{\mathrm{tr}}_v}\boldsymbol{\sigma}^{\mathrm{tr}}_{\mathrm{dev}} \tag{18a,b}$$

where analogously to Eq. (16.5) $(\sigma^{\mathrm{tr}}_v)^2=3/2\boldsymbol{\sigma}^{\mathrm{tr}}_{\mathrm{dev}}:\boldsymbol{\sigma}^{\mathrm{tr}}_{\mathrm{dev}}$ has been defined.

Upon inserting the relation (18b) into Eq. (5.2), the stress mode factor ξ can be expressed explicitly in terms of the trial stress tensor as

$$\begin{aligned}&1.\ \xi=\frac{\sqrt{27}}{2}\frac{J^{\mathrm{tr}}_3}{(J^{\mathrm{tr}}_2)^{3/2}},\quad \text{where}\\ &2.\ J^{\mathrm{tr}}_i=\frac{1}{i}\mathbf{1}:(\boldsymbol{\sigma}^{\mathrm{tr}}_{\mathrm{dev}})^i,\quad i=2,3\end{aligned} \tag{19}$$

However, further quantities such as ΔF_t or Δd_t have to be obtained iteratively. An inspection of the relations (16)–(19) reveals, that with knowledge of the quantities σ_v and d_t, which are determined in a local iteration described below, all remaining scalar and tensor quantities can directly be calculated.

5.2. Local iteration

The unknowns $\underline{x}=[\sigma_v,d_t]^{\mathrm{T}}$ appearing in Eqs. (16)–(19) are obtained from a nonlinear system of equations with dimension 2 as follows: Upon combining Eqs. (17.1) and (18b) we conclude that the unknown σ_v has to satisfy $\sigma_v=\sigma^{\mathrm{tr}}_v-3G\Delta F_t$. From this relation and the discretized damage update rule (15.2) the following nonlinear problem is derived:

$$\begin{aligned}&1.\ \underline{r}=[r_1,r_2]^{\mathrm{T}}=\underline{0},\quad \text{where}\\ &2.\ r_1=\sigma_v-\sigma^{\mathrm{tr}}_v+3G\Delta F_t\\ &3.\ r_2=\Delta d_t+{}^{n}d_t-d_t\end{aligned} \tag{20}$$

This problem can be solved iteratively with a Newton method

$$\underline{x}^{(k+1)}=\underline{x}^{(k)}-(\underline{J}^{(k)})^{-1}\underline{r}^{(k)},\quad \text{where}\quad \underline{J}^{(k)}=\left.\frac{\partial\underline{r}}{\partial\underline{x}}\right|_{\underline{x}^{(k)}},\quad k=0,1,2,\ldots. \tag{21a,b}$$

Alternative procedures for solution of local problems like (20) are given in Johansson et al. (1999) and furthermore in Mahnken (2000). The expressions for the elements of the Jacobian $\underline{J}$ can be extracted from the general variation $\delta\underline{r}$ summarized in Appendix A, and therefore we will not elaborate on more details at this stage.

Having solved the above local problem (20), the relations (15) are used for update of the history variables, and finally the deviatoric stresses are obtained from Eq. (18b).

5.3. Algorithmic tangent modulus

The algorithmic tangent modulus necessary for applying a Newton method for iterative solution of the global equilibrium problem requires the derivative of the stress tensor $\boldsymbol{\sigma}$ with respect to the total strain tensor $\boldsymbol{\varepsilon}$, i.e. $\mathbb{C}_{\mathrm{T}}=\mathrm{d}\boldsymbol{\sigma}/\mathrm{d}\boldsymbol{\varepsilon}$, see e.g. Simo and Hughes (1998) and references therein. Upon exploiting the variations in Appendix A straightforward differentiation renders the following result

$$\mathbb{C}_{\mathrm{T}}=\frac{2G\sigma_v}{\sigma^{\mathrm{tr}}_v}I\!I^{\mathrm{dev}}+\frac{3G\sigma_v}{(\sigma^{\mathrm{tr}}_v)^3}\boldsymbol{\sigma}^{\mathrm{tr}}_{\mathrm{dev}}\otimes\boldsymbol{\sigma}^{\mathrm{tr}}_{\mathrm{dev}}+\frac{1}{\sigma^{\mathrm{tr}}_v}\boldsymbol{\sigma}^{\mathrm{tr}}_{\mathrm{dev}}\otimes\frac{\mathrm{d}\sigma_v}{\mathrm{d}\boldsymbol{\varepsilon}}+B\mathbf{1}\otimes\mathbf{1} \tag{22}$$

The quantity $\mathrm{d}\sigma_v/\mathrm{d}\boldsymbol{\varepsilon}$ is part of the quantities $\mathrm{d}\underline{x}/\mathrm{d}\boldsymbol{\varepsilon}=[\mathrm{d}\sigma_v/\mathrm{d}\boldsymbol{\varepsilon},\mathrm{d}d_t/\mathrm{d}\boldsymbol{\varepsilon}]$, which in turn are obtained as follows: we consider the local problem (20) as an implicit function and conclude

$$\underline{r}[\boldsymbol{\varepsilon}, \underline{x}[\boldsymbol{\varepsilon}]] = \underline{0} \rightarrow \frac{\mathrm{d}\underline{r}}{\mathrm{d}\boldsymbol{\varepsilon}} = \frac{\partial \underline{r}}{\partial \boldsymbol{\varepsilon}} + \frac{\partial \underline{r}}{\partial \underline{x}} \frac{\mathrm{d}\underline{x}}{\mathrm{d}\boldsymbol{\varepsilon}} = \underline{0} \rightarrow \frac{\mathrm{d}\underline{x}}{\mathrm{d}\boldsymbol{\varepsilon}} = -\underline{J}^{-1} \frac{\partial \underline{r}}{\partial \boldsymbol{\varepsilon}} \tag{23a,b,c}$$

where $\underline{J}$ is the Jacobian defined in Eq. (21b). The expressions for $\partial \underline{r}/\partial \boldsymbol{\varepsilon}$ can be extracted from the general expression for the variation $\delta \underline{r}$ summarized in Appendix A, and therefore we will not elaborate on more details at this stage.

We close this section with the remark, that the local iteration procedure of the previous subsection and the algorithmic tangent modulus of this subsection has been implemented into the UMAT subroutine of the finite element program (ABAQUS-Version 6.3, 2002).

5.4. Some aspects on the sensitivity analysis for parameter identification

For parameter identification based on experimental testing a least-squares functional is considered as an identification criterion in order to minimize the distance of the simulated data to the experimental data. A general framework and technical details on application of a gradient based strategy for minimization of the least-squares functional is presented elsewhere, see Mahnken et al. (1998), and shall not be repeated here. For an analytical determination of the gradient a main objective becomes the determination of $\mathrm{d}^{n+1}\boldsymbol{\sigma}[\boldsymbol{\kappa}]/\mathrm{d}\boldsymbol{\kappa}$. At a further stage of the sensitivity analysis it is required to determine $\mathrm{d}\underline{x}[\boldsymbol{\kappa}]/\mathrm{d}\boldsymbol{\kappa}$. Following Mahnken et al. (1998), in the context of a time stepping, strain-controlled integration scheme the unknown vector $\underline{x}$ is the result of the local problem (20) thus satisfying the condition $\underline{r} = \underline{r}[\boldsymbol{\kappa}, \underline{x}, {}^n d_t, {}^n\boldsymbol{\varepsilon}, \boldsymbol{\varepsilon}_{\mathrm{dev}}] = \mathbf{0}$. Consequently the relations

$$\begin{aligned} &1.\ \frac{\mathrm{d}\underline{x}}{\mathrm{d}\boldsymbol{\kappa}} = -\underline{J}^{-1} \frac{\bar{\partial}\underline{r}}{\bar{\partial}\boldsymbol{\kappa}}, \quad \text{where} \\ &2.\ \frac{\bar{\partial}\underline{r}}{\bar{\partial}\boldsymbol{\kappa}} = \frac{\partial \underline{r}}{\partial \boldsymbol{\kappa}} + \frac{\partial \underline{r}}{\partial^n d_t} \frac{\partial^n d_t}{\mathrm{d}\boldsymbol{\kappa}} + \frac{\partial \underline{r}}{\partial^n \boldsymbol{\varepsilon}^{\mathrm{in}}} \frac{d^n \boldsymbol{\varepsilon}^{\mathrm{in}}}{\mathrm{d}\boldsymbol{\kappa}} + \frac{\partial \underline{r}}{\partial \boldsymbol{\varepsilon}_{\mathrm{dev}}} \frac{\mathrm{d}\boldsymbol{\varepsilon}_{\mathrm{dev}}}{\mathrm{d}\boldsymbol{\kappa}} \end{aligned} \tag{24}$$

can be derived, and where as before $\underline{J}$ is the Jacobian defined in Eq. (21b). Please observe the analogous structure of the relations (23c) and (24.1). The expressions for the quantities $\partial \underline{r}/\partial \boldsymbol{\kappa}$, $\partial \underline{r}/\partial^n d_t$, $\partial \underline{r}/\partial^n \boldsymbol{\varepsilon}^{\mathrm{in}}$, $\partial \underline{r}/\partial \boldsymbol{\varepsilon}_{\mathrm{dev}}$ can be extracted from the general variation $\delta \underline{r}$ summarized in Appendix A, and therefore we will not elaborate on more details at this stage. Furthermore, we remark, that the quantities $\mathrm{d}^n d_t/\mathrm{d}\boldsymbol{\kappa}$, $\mathrm{d}^n \boldsymbol{\varepsilon}^{\mathrm{in}}/\mathrm{d}\boldsymbol{\kappa}$, which give the result (24) a recursion structure, are obtained in a so-called *post-precessing* step, and it is noteworthy, that for the case of strain controlled experiments the quantity $\mathrm{d}\boldsymbol{\varepsilon}_{\mathrm{dev}}/\mathrm{d}\boldsymbol{\kappa}$ is zero. For the case of stress-controlled problems we also refer to the approach described in Mahnken et al. (1998).

6. Representative examples

6.1. Primary and secondary creep for aluminum alloy AK4-1T

In this section the primary and secondary creep phases for an aluminum alloy AK4-1T at a temperature of 473 K are simulated. The experimental data for this material were taken from Betten et al. (1998) and are shown in Fig. 3 under uniaxial tension, uniaxial compression and pure torsion, respectively. As noted in Betten et al. (1998) the equivalent inelastic strain is largest under pure torsion and smallest under uniaxial compression.

The simulation is done with the constitutive equations of Table 1, where $S = 3$ has been chosen for the number of modes, thus referring to the three types of experiments in tension, compression and shear, respectively. Note, that those parts of the model activating isotropic damage are not taken into account in this example. The results of the simulation are depicted in Fig. 3. A comparison with the experimental data

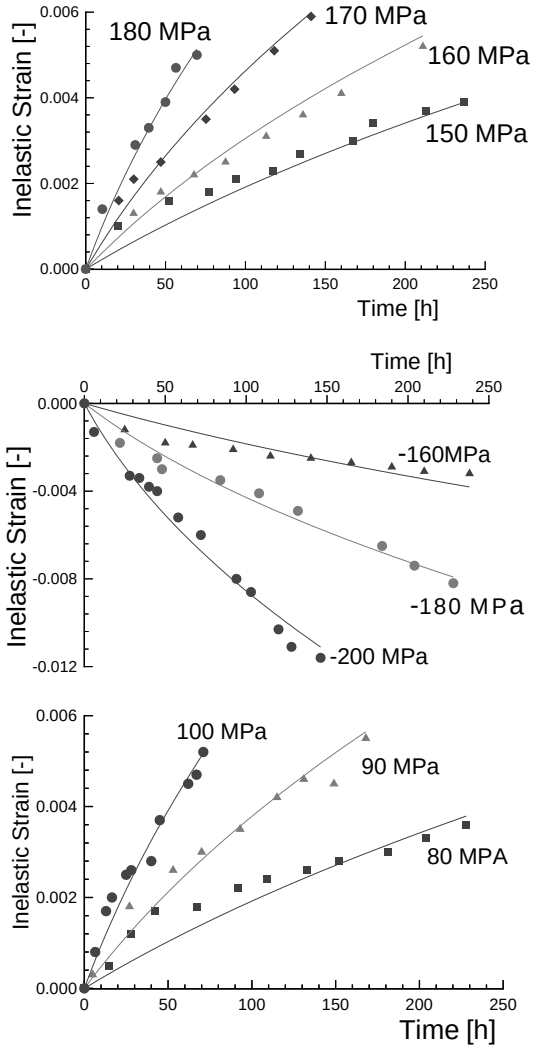

Fig. 3. Primary and secondary creep for AK4-1T: Comparison of simulation and experiment at 473 K under (top) tension, (middle) compression, and (bottom) torsion at various stress states. Symbols and lines refer to experimental and simulated data, respectively.

demonstrates the capability of the proposed model to simulate the different characteristic behaviors for all three stress modes.

Some remarks should be made concerning the strategy for obtaining the material parameters: These have been determined in a consecutive manner, where firstly only the data for the tension test were used, such that only the parameters A_1, n_1, q, s were allowed to vary. The optimization procedure started with some trial and error steps in order to overcome the local minima, followed by the gradient based strategy outlined in Section 5.4. In a second phase the compression data were added in order to vary the parameters A_2, n_2, q, s in the optimization process, and lastly the torsion data were taken into account to find solutions for A_3, n_3, q, s. In a fourth phase all parameters were allowed to vary thus giving the final solutions summarized in Table 2. From Table 2 it becomes apparent, that all three stress modes require individual sets of Norton parameters (A_i, n_i), $i = 1, 2, 3$ thus reflecting the *asymmetric* effects of the material.

Table 2
Primary and secondary creep for AK4-1T: Material parameters for tension, compression and torsion modes

B [GPa]	G [GPa]	σ_0 [MPa]	q [MPa]	s [–]	
83.3	25.75	5.15	40.31	70.0	
A_1 [–]	n_1 [–]	A_2 [–]	n_2 [–]	A_3 [–]	n_3 [–]
0.696	8.38	0.368	8.35	0.171	6.7

6.2. Primary, secondary and tertiary creep for superalloy René 95

This section intends to simulate experimental results for a superalloy René 95 at a temperature of 649 °C. The data for this material were taken from Stouffer and Dame (1996, p. 116) for a tension test and a compression test as shown in Fig. 4. Note, that the tension data exhibit a tertiary part, which is not observed in the compression test.

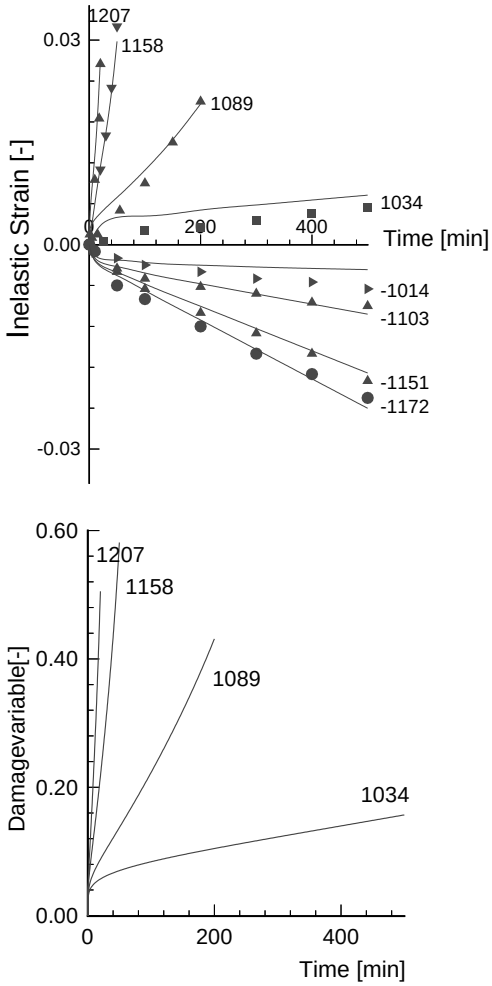

Fig. 4. Primary, secondary and tertiary creep for René 95: (top) Comparison of simulation and experiment for the inelastic strain under tension and compression at various stress states; (bottom) damage evolution for the tension tests. Symbols and lines refer to experimental and simulated data, respectively.

Table 3
Primary, secondary and tertiary creep for René 95: Material parameters corresponding to tension and compression modes

B [GPa]	G [GPa]	σ_0 [GPa]	q [MPa]	s [–]	
128.2	54.12	10.83	974.1	1158.2	
A_1 [–]	n_1 [–]	A_2 [–]	n_2 [–]	p_1 [–]	p_2 [–]
0.248	3.67	3.02d–3	2.5	3.5	0.0
B_1 [–]	m_1 [–]	B_2 [–]	m_2 [–]	q_1 [–]	q_2 [–]
3.6	1.0	0.0	–	1.0	–

The simulation is performed with the constitutive equations of Table 1, where $S = 2$ has been chosen for the number of modes, thus referring to the two types of experiments in tension and compression, respectively. Note, that the damage part is activated only for the tension mode. The comparison of the simulation in Fig. 4 with the experimental data illustrates, as in the previous example, the capability of the proposed model to simulate the different characteristic behaviors for both stress modes with a very satisfying agreement. In the second graph of Fig. 4 additionally the damage evolution is depicted.

The final results of the optimization process for all material parameters of Table 1 are summarized in Table 3. Analogously to the first example these were obtained in a consecutive manner, were firstly the compression data were used to obtain parameters for A_2, n_2, q, s. In a second phase the tension data were added thus obtaining estimates for A_1, n_1, q, s, B_1, m_1, p_1. In a third phase all parameters were allowed to vary thus giving the final solutions summarized in Table 3. As in the previous example it becomes apparent, that both stress modes require an individual set of Norton parameters (A_i, n_i), $i = 1, 2$ thus reflecting also here the asymmetric nature of the material.

6.3. Asymmetric relaxation effects in a square plate with circular hole

In this section the relaxation behavior of a square plate with circular hole shown in Fig. 5 is simulated with the finite element method. Due to obvious symmetry conditions only a quarter of the specimen is

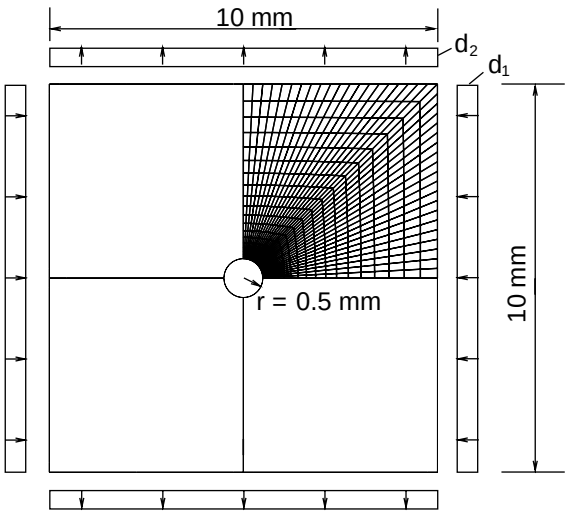

Fig. 5. Square plate with circular hole: Geometry, finite element discretization and loading.

considered in the plain strain calculation. The loading is displacement controlled, where the upper and lower sides of the specimen are moved outwards, whereas the left and the right sides are moved inwards. The values for the prescribed displacements are $d_1 = 0.015$ mm and the relaxation time is 1000 min. The same material as in the previous section is assumed, i.e. a superalloy René 95 at a temperature of 649 °C with material parameters of Table 3.

In the left upper plot of Fig. 6 the von Mises stress is depicted. This quantity is purely symmetric with respect to a 90° rotation of the plate, thus illustrating its incapability to detect asymmetric effects. In the top right plot of Fig. 6 the stress mode variable ξ is depicted at the beginning of loading ($t = 0.1$ min), thus illustrating the activation of tensile and compression regions. Along the rim of the hole, the model detects compression regimes at the upper and lower part of the hole, whereas at the right and left part tension regimes occur. The left bottom plot of Fig. 6 shows the equivalent inelastic strain e_v. Here, due to the comparatively small activation of damage the effect of asymmetry is almost negligible. In the right bottom plot of Fig. 6 the damage variable d_t is shown. Much larger values are adopted in the tension regimes compared to the compression regimes, thus illustrating the asymmetric effect.

Fig. 7 depicts the variation of von Mises stress σ_v and the damage variable d_t with respect to time. It becomes apparent that the former exhibits only small variations along the rim of the hole during the whole relaxation process. However, due to the different regimes of tension and compression the resulting damage

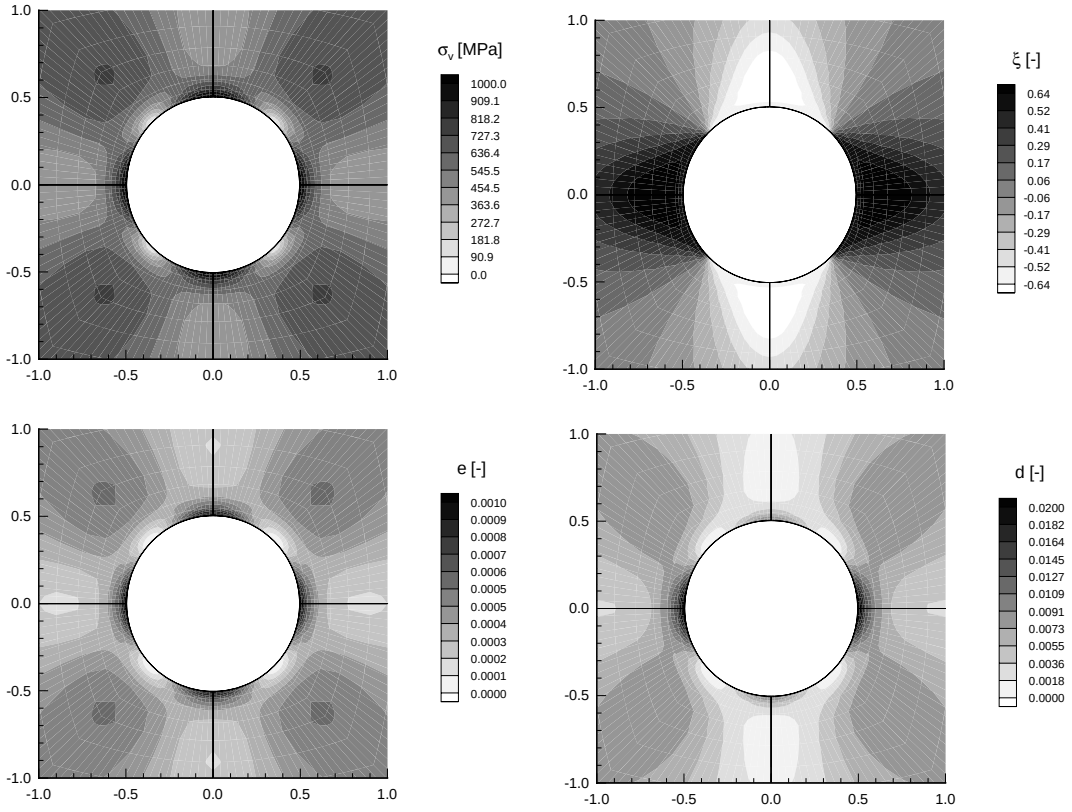

Fig. 6. Square plate with circular hole: (top left) von Mises stress σ_v and (top right) stress mode variable ξ at beginning of loading; (bottom left) equivalent plastic strain e_v and (bottom right) damage variable d_t at end of loading ($t = 1000$ min).

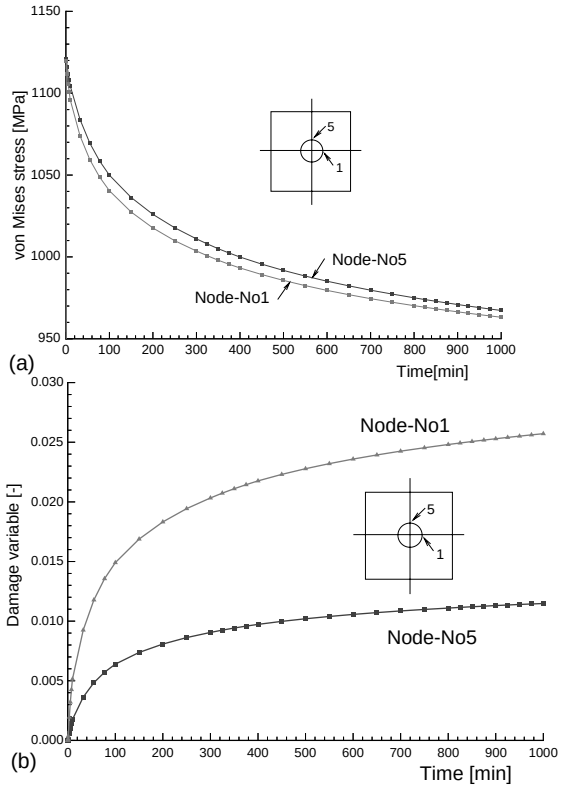

Fig. 7. Square plate with circular hole: (top) von Mises stress σ_v, (bottom) Damage variable d_t as a function of time at two nodes of the rim of hole.

variable becomes much larger at the right (and left) point of the hole compared to the upper (and lower) point of the hole during the relaxation process.

6.4. Gasturbine blade subjected to temperature and centrifugal loads

In this section a gasturbine blade with finite element discretization shown in Fig. 8 is investigated. This type of blade has been used formerly in gasturbine machines of ABB (now ALSTOM). The simulation is performed with the commercial program (ABAQUS-Version 6.3, 2002), where the constitutive equations of Table 1 have been implemented into the UMAT subroutine. Due to confidential agreement absolute values for the finite element results of temperature, stress, stress mode factor and damage factor are not given in the following result plots.

The component is subjected to thermal loading with temperature distribution in the left plot of Fig. 9 and centrifugal loading arising from rotation with 50 Hz. As in the previous section the superalloy René 95 is considered as the material. In order to take into account a (fictitious) temperature dependence, the factors of evolution for damage and equivalent plastic strain of Table 1 are multiplied with a (fictitious) factor

$$b = \exp\left(\frac{T - T_0}{\alpha T}\right) \tag{25}$$

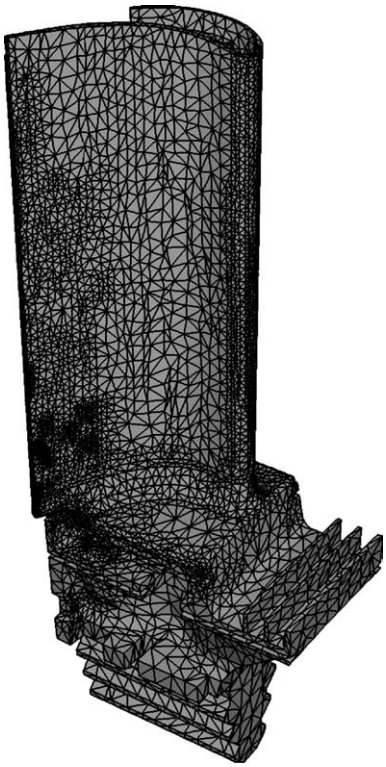

Fig. 8. Gasturbine blade: finite element discretization.

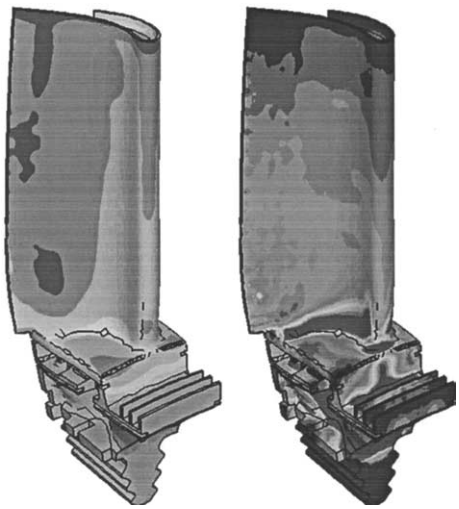

Fig. 9. Gasturbine blade: (Left) temperature distribution, dark areas in the pressure region correspond to hot areas. (Right) von Mises equivalent stress at beginning of loading, dark areas near the fillet region correspond to high stresses.

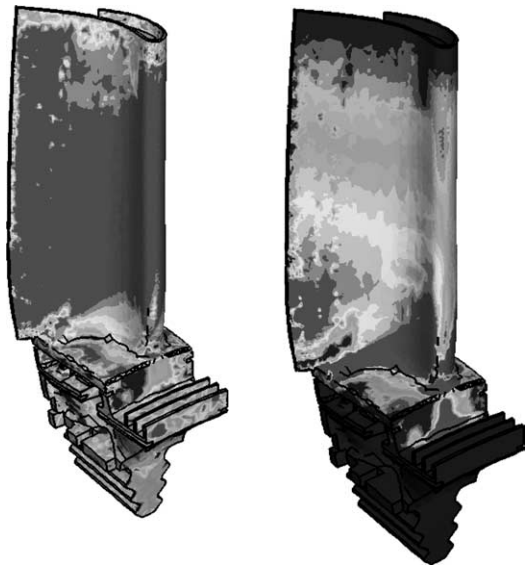

Fig. 10. Gasturbine blade: (Left) stress state variable ξ at beginning of loading, dark areas on the pressure side correspond to tension mode. (Right) damage variable d_t at end of loading ($t = 30000$ h), dark areas near the fillet region correspond to damaged areas.

Here T is the material temperature, $T_0 = 649$ °C is the temperature for the material parameters of Table 3 and $\alpha = 0.1$ has been chosen. Tetrahedral elements have been used in the finite element discretization such that the number of nodes is 184 248, the number of elements is 107 959 and the degrees of freedom is 552 744.

The right plot of Fig. 9 shows the von Mises equivalent stress at the beginning of loading after $t = 15$ min. The corresponding stress state variable ξ is depicted in the left plot of Fig. 10. It can be seen, that the combination of centrifugal and thermal loading results into the different tensile and compression regions. Naturally the tensile regions dominate, which is due to the centrifugal loading. The resulting damage variable d_t is shown in the right plot of Fig. 10. It becomes apparent that larger values are adopted in tension regimes with highest temperatures on the pressure side and near the fillet region with higher von Mises stresses.

7. Summary and conclusions

In this contribution a constitutive framework has been presented, which enables to simulate the creep deformation with characteristic behavior dependent on the loading state. The key idea here is an additive decomposition of the inelastic strain rate, where each of the quantities is weighted with a scalar valued function, which is dependent on the so-called stress mode angle. A main advantage of the concept is, that the stress modes can directly be associated to certain characteristic loading scenarios, such as tension, compression and shear, which are experimentally investigated in the laboratory.

In a further part of the paper the numerical implementation of the model equations is described, including the derivation of the algorithmic tangent operator for the equilibrium iteration and the sensitivity terms for parameter identification, each of them consistent with the underlying integration algorithm. The

integration algorithm and the algorithmic tangent operator have been implemented into the UMAT subroutine of the commercial finite element program (ABAQUS-Version 6.3, 2002).

Overall, the examples highlight the capability of the model to simulate asymmetric creep effects for two different materials, an aluminum alloy AK4 and a superalloy René 95. The latter material was also used to investigate the relaxation behavior of a square plate with circular hole and the evolution of creep damage in a large scale gasturbine blade.

The proposed approach is regarded as very general in order to simulate asymmetric effects for creep. Future work should take into account hydrostatic stress states, kinematic hardening and multiaxial stress states. Furthermore the aspects of damage induced anisotropy and finite strains will constitute an area of future research work.

Acknowledgements

The author is grateful to Alstom Power (LTD), Baden, Switzerland for provision of the finite element model of the gasturbine blade used in the example in Section 6.4.

Appendix A. Variations of significant quantities

In the sequel variations of significant quantities necessary for evaluation of the Jacobian (21b), the quantities $\partial \underline{r}/\partial \boldsymbol{\varepsilon}$ appearing on the r.h.s. in Eq. (23c) necessary for determination of the alogrithmic tangent modulus and the quantities $\bar{\partial} \underline{r}/\partial \boldsymbol{\kappa}$ appearing in Eq. (24), necessary for the sensitivity analysis are derived. In order to alleviate the derivations, the symbolic algebra program *MuPAD* (Gerhard et al., 2000) has been used on a *LINUX* platform. For completeness we remark that variations w.r.t. to the elastic constants G and B and to the scaling factor σ_0 are not taken into account.

Variation of $\boldsymbol{\sigma}^{\mathrm{tr}}_{\mathrm{dev}} = 2G(\boldsymbol{\varepsilon}_{\mathrm{dev}} - {}^{n}\boldsymbol{\varepsilon}^{\mathrm{in}})$

$$\delta \boldsymbol{\sigma}^{\mathrm{tr}}_{\mathrm{dev}} = 2G(\delta \boldsymbol{\varepsilon}_{\mathrm{dev}} - \delta {}^{n}\boldsymbol{\varepsilon}^{\mathrm{in}}) \tag{A.1}$$

Variation of $J^{\mathrm{tr}}_i = \frac{1}{i}\mathbf{1} : (\boldsymbol{\sigma}^{\mathrm{tr}}_{\mathrm{dev}})^i, \quad i = 1,2,3$

$$\delta J^{\mathrm{tr}}_i = (\boldsymbol{\sigma}^{\mathrm{tr}}_{\mathrm{dev}})^{i-1} : \delta \boldsymbol{\sigma}^{\mathrm{tr}}_{\mathrm{dev}}, \quad i = 1,2,3 \tag{A.2}$$

Variation of $\sigma^{\mathrm{tr}}_v = \left(\frac{3}{2}\boldsymbol{\sigma}^{\mathrm{tr}}_{\mathrm{dev}} : \boldsymbol{\sigma}^{\mathrm{tr}}_{\mathrm{dev}}\right)^{1/2} = \sqrt{3J^{\mathrm{tr}}_2}$

$$\delta \sigma^{\mathrm{tr}}_v = \frac{3}{2\sigma^{\mathrm{tr}}_v}\delta J^{\mathrm{tr}}_2 \tag{A.3}$$

Variation of $\boldsymbol{\sigma}_{\mathrm{dev}} = \frac{\sigma_v}{\sigma^{\mathrm{tr}}_v}\boldsymbol{\sigma}^{\mathrm{tr}}_{\mathrm{dev}}$

$$\delta \boldsymbol{\sigma}_{\mathrm{dev}} = \frac{1}{\sigma^{\mathrm{tr}}_v}\boldsymbol{\sigma}^{\mathrm{tr}}_{\mathrm{dev}}\delta\sigma_v - \frac{\sigma_v}{\left(\sigma^{\mathrm{tr}}_v\right)^2}\boldsymbol{\sigma}^{\mathrm{tr}}_{\mathrm{dev}}\delta\sigma^{\mathrm{tr}}_v + \frac{\sigma_v}{\sigma^{\mathrm{tr}}_v}\delta\boldsymbol{\sigma}^{\mathrm{tr}}_{\mathrm{dev}} \tag{A.4}$$

Variation of $\xi = \frac{\sqrt{27}}{2}\frac{J^{\mathrm{tr}}_3}{(J^{\mathrm{tr}}_2)^{3/2}}$

$$\delta\xi = \frac{\sqrt{27}}{2}\frac{\delta J^{\mathrm{tr}}_3}{(J^{\mathrm{tr}}_2)^{3/2}} - \frac{3\sqrt{27}}{4}\frac{\delta J^{\mathrm{tr}}_3}{(J^{\mathrm{tr}}_2)^{5/2}}\delta J^{\mathrm{tr}}_2 \tag{A.5}$$

Variations of $w_1[\xi]$, $w_2[\xi]$, $w_3[\xi]$ (see Eq. (11))

$$\begin{aligned}
&1.\ \delta w_1[\xi] = \begin{cases} 2\xi\delta\xi, & \text{if } \xi \geqslant 0 \\ 0, & \text{else} \end{cases} \\
&2.\ \delta w_2[\xi] = \begin{cases} 0, & \text{if } \xi \leqslant 0 \\ 2\xi\delta\xi, & \text{else} \end{cases} \\
&3.\ \delta w_3[\xi] = -2\xi\delta\xi
\end{aligned} \tag{A.6}$$

Variation of $R = q(1 - \exp(-se_v))$

$$\delta R = \delta q(1 - \exp(-se_v)) + q\exp(-se_v)(\delta s e_v + s\delta e_v) \tag{A.7}$$

Variation of $\Delta F_i = \Delta t A_i (\frac{\sigma_{\text{dev}} - R}{\sigma_0})^{n_i} (\frac{1}{1-d_t})^{p_i}$

$$\begin{aligned}
\delta\Delta F_i = {} & \Delta t A_i n_i \left(\frac{\sigma_{\text{dev}} - R}{\sigma_0}\right)^{n_i - 1} \left(\frac{1}{1-d_t}\right)^{p_i} (\delta\sigma_{\text{dev}} - \delta R) + \Delta F_i \log\left(\frac{\sigma_{\text{dev}} - R}{\sigma_0}\right)\delta n_i \\
& + \Delta F_i \log\left(\frac{1}{1-d_t}\right)\delta p_i + \Delta t \delta A_i \left(\frac{\sigma_{\text{dev}} - R}{\sigma_0}\right)^{n_i} \left(\frac{1}{1-d_t}\right)^{p_i} \\
& + \Delta t p_i A_i \left(\frac{\sigma_{\text{dev}} - R}{\sigma_0}\right)^{n_i} \left(\frac{1}{1-d_t}\right)^{p_i - 1} \frac{1}{(1-d_t)^2}\delta d_t
\end{aligned} \tag{A.8}$$

Variation of $\Delta F_t = \sum_{i=1}^{S} \Delta F_i w_i$

$$\delta\Delta F_t = \sum_{i=1}^{S} \delta\Delta F_i w_i + \sum_{i=1}^{S} \Delta F_i \delta w_i \tag{A.9}$$

Variation of $\Delta d_t = \Delta t B_i (\frac{\sigma_{\text{dev}}}{\sigma_0})^{m_i} (\frac{1}{1-d_t})^{q_i}$

$$\begin{aligned}
\delta\Delta d_i = {} & \Delta t B_i m_i \left(\frac{\sigma_{\text{dev}}}{\sigma_0}\right)^{m_i - 1} \left(\frac{1}{1-d_t}\right)^{q_i} \delta\sigma_{\text{dev}} + \Delta d_t \log\left(\frac{\sigma_{\text{dev}}}{\sigma_0}\right)\delta m_i + \Delta d_t \log\left(\frac{1}{1-d_t}\right)\delta q_i \\
& + \Delta t \delta B_i \left(\frac{\sigma_{\text{dev}}}{\sigma_0}\right)^{m_i} \left(\frac{1}{1-d_t}\right)^{q_i} + \Delta t q_i B_i \left(\frac{\sigma_{\text{dev}}}{\sigma_0}\right)^{m_i} \left(\frac{1}{1-d_t}\right)^{q_i - 1} \frac{1}{(1-d_t)^2}\delta d_t
\end{aligned} \tag{A.10}$$

Variation of $\Delta d_t = \sum_{i=1}^{S} \Delta d_i w_i$

$$\delta\Delta d_t = \sum_{i=1}^{S} \delta\Delta d_i w_i + \sum_{i=1}^{S} \Delta d_i \delta w_i \tag{A.11}$$

Variation of $\Delta e = \Delta F_t$

$$\delta\Delta e = \delta\Delta F_t \tag{A.12}$$

Variation of $r_1 = \sigma_v - \sigma_v^{\text{tr}} + 3G\Delta F_t$

$$\delta r_1 = \delta\sigma_v - \delta\sigma_v^{\text{tr}} + 3G\delta\Delta F_t \tag{A.13}$$

Variation of $r_2 = \Delta d_t + {}^n d_t - d_t$

$$\delta r_2 = \delta\Delta d_t + \delta^n d_t - \delta d_t \tag{A.14}$$

References

ABAQUS-Version 6.3, Users Manual, Hibbett, Karlsson & Sorensen, Inc., 2002.

Altenbach, H., 2001. Consideration of stress state influences in the material modelling of creep and damage. In: Murakami, S., Ohno, N. (Eds.), Fifth IUTAM-Symposium on Creep in Structures. Kluwer, Dordrecht, pp. 141–150.

Altenbach, H., Altenbach, J., Zolochevsky, A., 1995. Erweiterte Deformations modelle und Versagenskriterien der Werkstoffmechanik. Deutscher Verlag für Grund stoffindustrie, Stuttgart.

Ashby, M.F., Jones, D.R.H., 1996. Engineering Materials, second ed. Butterworth-Heinemann, Oxford.

Betten, J., 2001. Mathematical modelling of materials behavior under creep conditions. Appl. Mech. Rev. 54 (2), 107–132.

Betten, J., Sklepus, S., Zolochevsky, A., 1998. A creep damage model for initially isotropic materials with different properties in tension and compression. Eng. Fract. Mech. 59 (5), 623–641.

Betten, J., Sklepus, S., Zolochevsky, A., 1999. A microcrack description of creep damage in crystallin solids with different behaviour in tension and compression. Int. J. Damage Mech. 8, 197–232.

Dieter, G.E., 1988. Mechanical Metallurgy. McGraw-Hill Book Company, London.

Ehlers, W., 1995. A single-surface yield function for geomaterials. Arch. Appl. Mech. 65, 246–259.

Gerhard, J., Oevel, W., Postel, F., Wehmeier, S., 2000. Mupad Tutorial. Springer-Verlag, Berlin.

Johansson, M., Mahnken, R., Runesson, K., 1999. Efficient integration technique for generalized viscoplasticity coupled to damage. Int. J. Numer. Meth. Eng. 44, 1727–1747.

Mahnken, R., 2000. A comprehensive study of a multiplicative elastoplasticity model coupled to damage including parameter identification. Comp. Struct. 74 (2), 179–200.

Mahnken, R., 2001. Strength difference in compression and tension and pressure dependence of yielding in elasto-plasticity. Comp. Meth. Appl. Mech. Eng. 190, 5057–5080.

Mahnken, R., 2002. Anisotropic creep modeling based on elastic projection operators with applications to CMSX-4 superalloy. Comp. Meth. Appl. Mech. Eng. 191, 1611–1637.

Mahnken, R., Johansson, M., Runesson, K., 1998. Parameter estimation for a viscoplastic damage model using a gradient-based optimization algorithm. Eng. Comput. 15 (7), 925–955.

Poirier, J.-P., 1985. Creep of Crystals, High-Temperature Deformation Processes in Metals, Ceramics and Minerals. Cambridge University Press, Cambridge.

Riedel, J., 1987. Fracture at High Temperatures. Springer-Verlag, Berlin.

Simo, J.C., Hughes, T.J.R., 1998. Computational Inelasticity. In: Interdisciplinary Applied Mathematics. In: Mechanics and Materials, Vol. 7. Springer-Verlag.

Spitzig, W.A., Sober, R.J., Richmond, O., 1975. Pressure dependence of yielding and associated volume expansion in tempered martensite. Acta. Metall. 23, 885–893.

Stouffer, D.C., Dame, L.T., 1996. Inelastic Deformation of Metals. John Wiley & Sons, New York.

Voyiadjis, G.Z., Zolochevsky, A., 1998. Modeling of secondary creep behaviour for anisotropic materials with different properties in tension and compression. Int. J. Plast. 14 (10–11), 388–399.

Voyiadjis, G.Z., Zolochevsky, A., 2000. Modeling of secondary creep behaviour for anisotropic materials with different properties in tension and compression. Int. J. Solids Struct. 37, 3281–3303.

Zolochevskii, A.A., 1989. Modification of the theory of plasticity of materials differently resistant to tension and compression for simple loading processes. Soviet Appl. Mech. (Transl. Prikladnaya Mekhanika) 24 (12), 1212–1217.

Zolochevskii, A.A., 1990. Method of calculating the strength of mine pipes formed from materials that behave differently under tension and compression. Strength Mater. (Transl. Problemy Prochnosti) 22 (3), 422–428.

Zolochevsky, A.A., 1991. Creep of isotropic and anisotropic materials with different behaviour in tension and compression. In: Zyczkovski, M. (Ed.), Creep in Structures. Springer-Verlag, Berlin, pp. 217–220.